Volume 2
Number 6
November 2025
Pages 775–938

RSC Mechanochemistry

rsc.li/RSCMechanochem

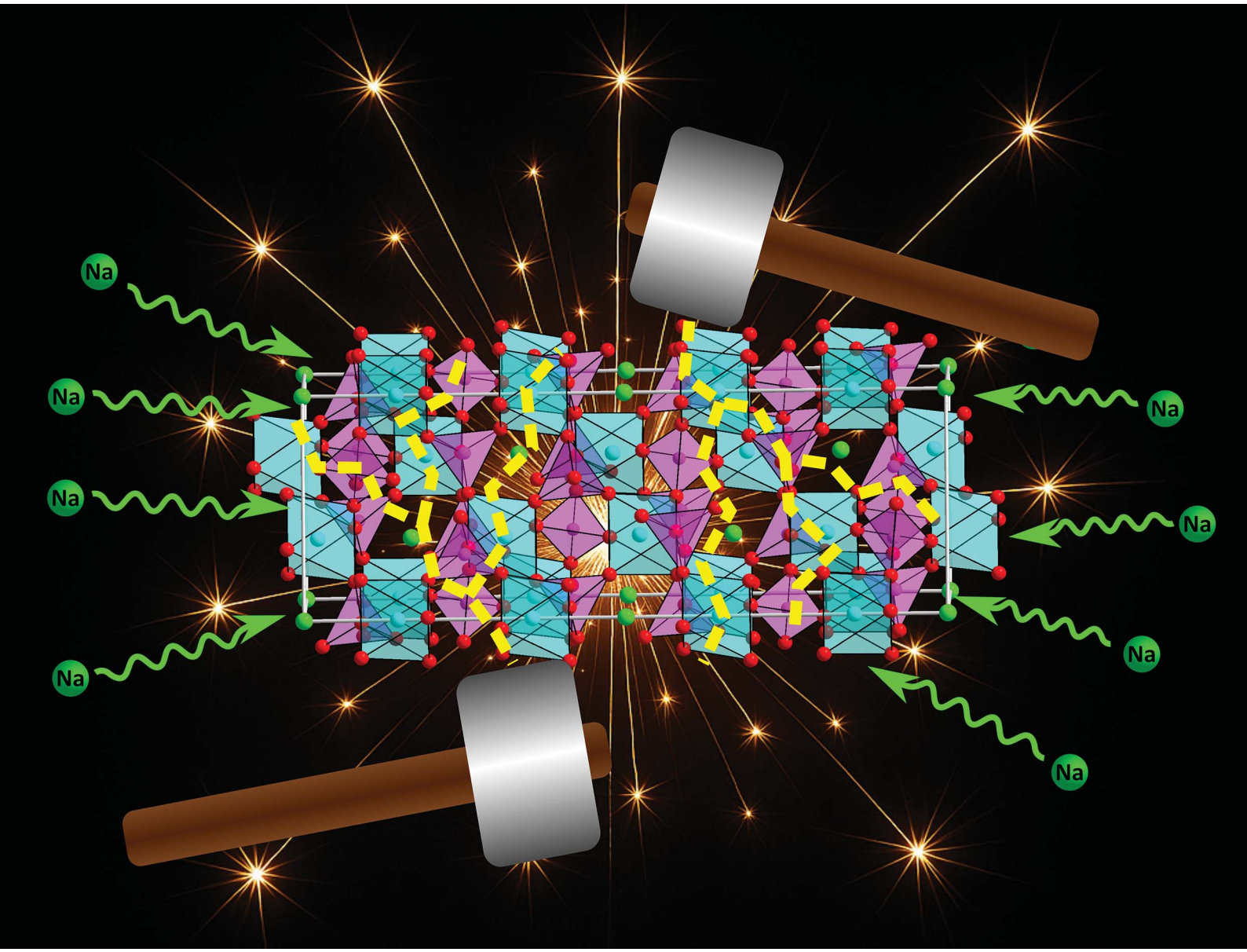

ISSN 2976-8683

ROYAL SOCIETY OF CHEMISTRY

PAPER

Guido Kickelbick *et al.*

Mechanochemical activation and sodium intercalation in the $NaTi_2(PO_4)_3$ NASICON structure

RSC Mechanochemistry

ROYAL SOCIETY OF CHEMISTRY

PAPER

View Article Online
View Journal | View Issue

Cite this: *RSC Mechanochem.*, 2025, **2**, 813

Mechanochemical activation and sodium intercalation in the $NaTi_2(PO_4)_3$ NASICON structure

Tobias Benjamin Straub, [a] Elias C. J. Gießelmann [a] and Guido Kickelbick *[ab]

$NaTi_2(PO_4)_3$, a NASICON-type sodium titanium phosphate (NTP), is a promising candidate for sodium-ion energy storage due to its robust structural and electrochemical properties. This study explores the impact of mechanochemical activation (MCA) on NTP synthesized *via* high-temperature methods, with a focus on sodium intercalation behaviour under various milling conditions. Sodiation experiments were performed in suspension using different sodium sources and the resulting structural and compositional changes after activation and the mean sodium content ($\langle x \rangle$ defined as the average number of sodium ions per formula unit in $Na_xTi_2(PO_4)_3$) were determined by powder X-ray diffraction (PXRD) combined with Rietveld refinement as well as scanning electron microscopy (SEM), physisorption isotherm measurements, inductively coupled plasma mass spectrometry (ICP-MS), Raman spectroscopy and solid-state NMR. While MCA did not induce a phase transformation, extended milling times led to reduced crystallite sizes and increased structural disorder. The extent of sodium incorporation was strongly influenced by both the milling duration and the chemical nature of the sodium source, particularly its ability to reduce titanium. The highest sodium content of 3.5 approaching the theoretical maximum of 4.0 ($Na_4Ti_2(PO_4)_3$) was achieved using sodium naphthalene as the sodiation reagent.

Received 1st July 2025
Accepted 1st October 2025

DOI: 10.1039/d5mr00090d

rsc.li/RSCMechanochem

Introduction

Lithium-based materials have long dominated the field of energy storage, powering a wide range of technologies from portable electronics to electric vehicles and large-scale grid systems.[1] However, the finite nature of lithium resources, coupled with rapidly increasing global demand, has raised concerns about long-term sustainability and supply security. Forecasts consistently predict a sharp rise in lithium consumption, intensifying the need for alternative energy storage solutions.[2,3] Sodium has emerged as a compelling substitute for lithium, offering several key advantages. It is significantly more abundant in the Earth's crust – approximately 23.6×10^3 mg kg^{-1} compared to just 20 mg kg^{-1} for lithium[4] – and is more economically accessible. These attributes make sodium-based systems particularly attractive for large-scale and cost-sensitive applications.[5]

Sodium is already utilized in various energy storage technologies, including high-temperature systems such as sodium-sulfur batteries and Zero Emission Battery Research Activities (ZEBRA) cells, both of which employ molten sodium. Furthermore, sodium-ion batteries, which operate at ambient temperatures, are gaining traction as a viable alternative to lithium-ion systems, with sodium serving as both anode and cathode material.[6]

Among the various materials explored for sodium-based energy storage, NASICON-type compounds (an acronym for sodium (Na) super ionic conductors), with the general formula $NaM_2(PO_4)_3$ where M = Zr, Ti, or Ge, offer one of the promising alternatives within the broader field of sodium-based energy storage technologies. These structures were initially described by Hagman and Kierkegaard in 1968.[7] The zirconium-containing compound $NaZr_2(PO_4)_3$ served as a prototype for the structural description, but there are also other isostructural compounds, such as those containing titanium, germanium, and hafnium.[8] The term "NASICON-type structure" describes double phosphates with the general formula $A_xB_y(PO_4)_3$, where A is not restricted to sodium, but can also include other alkali and alkaline earth metals, while B can be a transition or a non-transition element in the trivalent, tetravalent, or pentavalent state.[9–11] NASICON-type structures crystallize in a rhombohedral three-dimensional framework composed of PO_4 tetrahedra that share corners with BO_6 octahedra, forming the so-called lantern units. These structural units consist of three PO_4 tetrahedra connected to two BO_6 octahedra by corner-sharing oxygen atoms, creating two different interstitial sites where the alkali ions are located.[7,11–17] Fig. 1 illustrates the lantern unit and the corresponding unit cell structure using NTP as a representative example.

Goodenough *et al.* demonstrated that NASICON-type structures exhibit good properties as solid electrolytes in high energy

[a]*Saarland University, Inorganic Solid-State Chemistry, Campus, Building C4.1, 66123 Saarbrücken, Germany. E-mail: guido.kickelbick@uni-saarland.de*
[b]*Saarene – Saarland Center for Energy Materials and Sustainability, Campus C4.2, 66123 Saarbrücken, Germany*

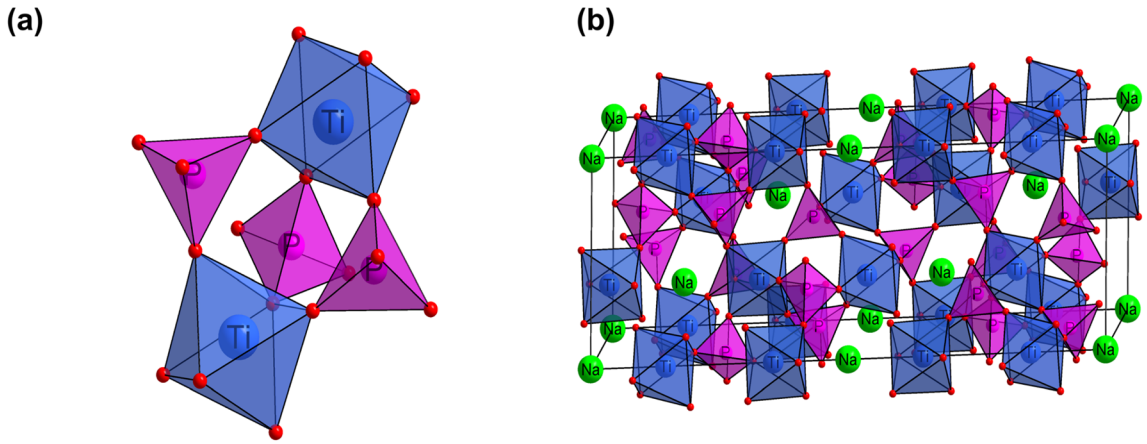

Fig. 1 The lantern unit (a) and the unit cell (b) of a NASICON-structure, shown here using the example of $NaTi_2(PO_4)_3$ (Ti: blue, P: pink, O: red, Na: green).

density batteries,[18] leading to numerous investigations aimed at determining the diffusion mechanisms or improving the ionic and/or electrical conductivity.[12,17,19,20]

Due to the larger ionic radius of Na^+ (102 pm) compared to Li^+ (76 pm), the intercalation and deintercalation of sodium in electrode materials often leads to challenges such as poor transport kinetics and structural degradation.[20–24] Sodium titanium phosphate ($NaTi_2(PO_4)_3$) as a typical representative of the NASICON-type structure family enables reversible intercalation and deintercalation of sodium with zero-strain or little lattice strain due to its large interstitial sites. This leads to good structural stability, rapid insertion and extraction of Na^+, a relatively high theoretical charge capacity of 133 mAh g^{-1} and high Na ion conductivity.[17,25–31] In contrast to other NASICON-type structures, sodium titanium phosphate, which crystallizes in the highly symmetric rhombohedral γ-phase (space group $R\bar{3}c$), does not undergo phase transformations at elevated temperatures. However, it exhibits a thermal expansion of the lattice parameter up to 1000 °C.[14,32–36]

Various synthesis methods have been employed to produce NTP, including high-temperature solid-state reactions using different precursors,[9,25,35] solvothermal synthesis,[20,26,27] the Pechini method,[28] microwave assisted synthesis,[37] coprecipitation from aqueous solution[38] and the sol–gel method.[29] These typically yield thermodynamically stable, defect-free materials.

Upon chemical or electrochemical sodiation, NTP can form sodium-rich phases $Na_{1+x}Ti_2(PO_4)_3$ ($0 \leq x \leq 3$), involving stepwise reduction of Ti^{4+} to Ti^{3+} and subsequently to Ti^{2+}. The $Na_2Ti_2(PO_4)_3$ phase ($x = 1$) can be obtained by chemical intercalation at high temperature. However, due to the instability of this phase, a disproportionation reaction occurs upon cooling, resulting in the formation of the two phases $NaTi_2(PO_4)_3$ and $Na_3Ti_2(PO_4)_3$. Delmas *et al.* were among the first to carry out experiments on the intercalation of sodium in $NaTi_2(PO_4)_3$. They used elemental sodium at high temperature in an evacuated quartz ampoule or sodium naphthalene at room temperature in THF as intercalation agents.[17,35,36,39] Temperature-dependent structural phase transitions in $Na_3Ti_2(PO_4)_3$ are well documented, showing reversible changes from the low-temperature alpha phase to the high-temperature gamma phase around 85 °C.[14] Various structural models have been proposed for $Na_3Ti_2(PO_4)_3$ and $Na_4Ti_2(PO_4)_3$, with many theoretical studies focusing on symmetry and charge ordering.[36] $Na_3Ti_2(PO_4)_3$ adopts a low-symmetry triclinic ($P\bar{1}$) structure in the alpha phase. For $Na_4Ti_2(PO_4)_3$, theory predicts a symmetry reduction compared to the rhombohedral $NaTi_2(PO_4)_3$ parent structure due to mixed Ti^{3+}/Ti^{2+} valence states to the $R32$ space group. However, experimental evidence, including work by Senguttuvan *et al.* on electrochemically prepared samples, primarily supports the high-symmetry rhombohedral $R\bar{3}c$ structure for $Na_4Ti_2(PO_4)_3$.[16] The symmetry reduction remains a theoretical prediction awaiting clear experimental confirmation to our best knowledge.

Mechanochemical activation (MCA), particularly *via* high-energy ball milling (hebm), has emerged as a powerful technique to modify material properties. MCA can reduce particle and crystallite sizes, increase surface area and reactivity, introduce structural disorder, and even induce amorphization.[40–43] Hebm of solids can lead to the conversion of reactants,[44–46] phase transitions,[47,48] or the formation of metastable phases, often associated with an increased defect concentration.[49–51] Mechanochemistry also has other advantages such as the absence of solvents,[52] lower reaction temperatures,[40] shorter reaction times,[53] and the reduction of by-products.[45] The release of oxygen and the associated formation of oxygen vacancies in the crystal lattice is another effect of hebm and is described in the literature for $ZnFe_2O_4$, MnO_2 or $LiNbO_3$, for example.[54–56] Today, MCA is successfully used in the various processes, such as: activating magnesium for usage in solid-state fluoro-Grignard reactions, improving the leaching of arsenic from copper smelting flue dusts, extracting lithium and cobalt from spend lithium-ion batteries and enhancing the sodium-ion storage behaviors in $TiNb_2O_7$.[57–60]

An attractive way to analyze the effects of mechanochemical activation on the NASICON-type structures is the chemical intercalation of sodium in suspension into the host materials

after their MCA. Typical sodiation reagents include biphenyl sodium, sodium naphthalene, sodium sulfide, and sodium iodide, which differ in their sodiation potential.[35,61–66]

Ball milling is frequently used for the synthesis and modification of NASICON-type structures. It is often used for mixing the reactants before a high-temperature synthesis or for additional homogenization and simultaneous reduction of the particle size between calcination steps.[16,67,68] The process is also often applied in the production of carbon-coated composite materials. For example, glucose or sucrose can be milled together with the previously produced NASICON-type structure powders and then calcined.[11,69] However, there is very little literature on the subject of mechanochemical activation of NASICON-type structures or analyses of their material properties in combination with ball milling. Snarskis *et al.* used ball milling to achieve a uniform particle size distribution of the material, enabling the observation of the influence of the two different synthesis routes employed on its properties.[70] Park *et al.* investigated the electrochemical properties of $NaTi_2(PO_4)_3$ as an anode material, focusing on three variants: the untreated NTP, the carbon-coated $NaTi_2(PO_4)_3$ prepared by ball milling, and the carbothermally annealed NTP.[28] Li *et al.* have published a study on the influence of particle size on the microstructure and ionic conductivity of $Li_{1.3}Al_{0.3}Ti_{1.7}(PO_4)_3$, while Chong *et al.* have investigated the same properties in $Na_3Zr_2(SiO_4)_2PO_4$.[71,72] Novikova *et al.* investigated the influence of MCA on physical parameters of $Li_{1+x}Hf_{2-x}In_x(PO_4)_3$ (x = 0, 0.05, 0.1) such as crystallite size, particle size and specific surface area. They could show that the mechanochemically activated samples exhibit catalytic activity for ethanol dehydration reactions in ethanol conversion reactions.[73]

In this study, we systematically investigate the influence of mechanochemical activation on the physical properties and sodium intercalation behavior of $NaTi_2(PO_4)_3$ synthesized *via* high-temperature methods. We hypothesize that sodium uptake is strongly influenced by crystallite size, surface area, and defect concentration—parameters that are modulated by MCA. By varying milling conditions and sodiation reagents, we aim to elucidate the relationship between activation parameters and sodium intercalation efficiency, providing new insights into the design of high-performance NASICON-type materials for sodium-ion storage.

Experimental section

Materials

Titanium dioxide (anatase, 99.5%, ChemPUR, Karlsruhe, Germany), diammonium hydrogen phosphate (98%, Thermo Scientific, Kandel, Germany), sodium dihydrogen phosphate (p.a., Merck, Darmstadt, Germany), acetonitrile (>99.9%, Th. Geyer, Renningen, Germany), 2-propanol (97%, Biesterfeld Spezialchemie, Hamburg, Germany), sodium (99.8%, Acros, Geel, Belgium), naphthalene (99+%, Alfa Aesar, Karlsruhe, Germany), tetrahydrofuran (99.9+%, Th. Geyer, Renningen, Germany), *n*-pentane (99%, Stockmeier Chemie, Bielefeld, Germany), sodium iodide anhydrous (Riedel-de Haën, Seelze, Germany) and sodium sulfide nonahydrate (98+%, Acros, Geel, Belgium). $Na_2S{\cdot}9H_2O$ was slowly heated up to 110 °C under vacuum for several days to remove the crystal water.[64]

All received solid reactants were characterized by X-ray powder diffraction before use. Solvents were purified and dried using a Solvent Purification System (MBRAUN, Garching, Germany) and stored under argon and over molecular sieves. All chemicals were used as received without further purification.

Oven-equipment

Muffle furnace N11/HR (Nabertherm, Lilienthal, Germany) equipped with a C30 control unit and with a maximum temperature of 1280 °C.

Characterization

Powder X-ray diffraction (PXRD) patterns of the pulverized samples were recorded at room temperature on a D8-A25-Advance diffractometer (Bruker, Karlsruhe, Germany) in Bragg–Brentano θ–θ-geometry (goniometer radius 280 mm) with Cu K_α-radiation (λ = 154.0596 pm). A 12 μm Ni foil working as K_β filter and a variable divergence slit were mounted at the primary beam side. A LYNXEYE detector with 192 channels was used at the secondary beam side. Experiments were carried out in a 2θ range of 7 to 120° with a step size of 0.013° and a total scan time of 2 hours. The background caused by white radiation and sample fluorescence was reduced by limiting the energy range of the detection. The recorded data were analysed with the Bruker TOPAS 5.0 software using the Rietveld refinement.[74] The mean crystallite size was calculated at the mean volume weighted column height derived from the integral breadth (L_{Vol}-IB). Instrumental broadening and strain were considered.

The required structure files were obtained from the relevant literature or the Pearson's Crystal database.[75]

The nitrogen sorption analyses at −196 °C were carried out using a Quadrasorb EVO system (Quantachrome Instruments, Boynton Beach, USA). Before each measurement, the materials were outgassed for 10 hours at 100 °C under vacuum using a XeriPrep™ degasser (Quantachrome Instruments, Boynton Beach, USA). The adsorption and desorption isotherms were recorded, and the specific surface area was determined using the BET method in the relevant pressure range p/p_0 of 0.05 to 0.3.

The elemental quantification was conducted *via* inductively coupled plasma mass spectrometry with a commercial ICP-MS system (8900 Triple Quad and SPS4 autosampler, Agilent, Santa Clara, USA). Stock solutions of single element ICP-MS standards of Na (Merck KGaA, Darmstadt, Germany), Ti (VWR International Ltd, Leicestershire, England), Zr (Merck Millipore, Darmstadt, Germany), Y (Merck Millipore, Darmstadt, Germany), Ho (Merck KGaA, Darmstadt, Germany) and Sc (Merck Millipore, Darmstadt, Germany) were used. The detector dwell time was 100 μs the repetition was 3 times, and the measured isotopes were ^{23}Na, ^{47}Ti, ^{90}Zr, ^{89}Y as well as ^{45}Sc and ^{165}Ho as internal standard. For the ICP-MS measurements, approx. 5 mg of the sample were dissolved in 1 mL hydrofluoric acid (48%, Merck KGaA, Darmstadt, Germany) and diluted with ultrapure water. An external calibration was done for quantification.

For the acquisition of the scanning electron microscopy images, the sample was mounted on a carbon adhesive film and then sputtered with a thin layer of gold. The images were taken with the microscope model JSM-7000 F (JEOL, Tokyo, Japan), the working distance was 10 mm, and a voltage of 20 kV was applied.

Solid-state single-pulse MAS NMR spectra were recorded on an Avance III HD-Ascend 400WB spectrometer (Bruker, Billerica, USA) at 295 K using 4 mm inner diameter ZrO_2 rotors with a 13 kHz rotation frequency and a relaxation delay of 1 s for ^{23}Na and 3 s for ^{31}P. The resonance frequencies were 105.89 MHz for ^{23}Na NMR spectra and 162.04 MHz for ^{31}P NMR spectra. Aqueous NaCl solution (1 M) was used as external reference at 0 ppm for sodium and phosphorus was referenced against $NH_4H_2(PO_4)$. Spectra were recorded using the TopSpin software.[76] Fitting of the spectra was performed using the DMFit software program package.[77]

The recording of the Raman spectra was performed on Horiba Modular spectrometer (Horiba Scientific, Kyoto, Japan) equipped with a 532 nm neodymium-doped yttrium-aluminium-garnet laser, a fibre optic coupled SuperHead Raman probe head, a sample chamber and a 1800 lines per mm grating was used.

All structural drawings were created with the Diamond 4 software (Crystal Impact, Bonn, Germany).[78]

Synthesis

Solid-state synthesis of $NaTi_2(PO_4)_3$. $NaTi_2(PO_4)_3$ was synthesized by a slightly modified solid-state reaction compared to the original literature, resulting in a white powder as the product.[35,37,79] Initially, 3.96 g titanium dioxide (2 equivalents), 6.49 g diammonium hydrogen phosphate (2 equivalents) and 2.97 g sodium dihydrogen phosphate (1 equivalent) were homogenized in a planetary ball mill (PM 100, Retsch, Haan, Germany) by wet milling with *n*-pentane (35 mL) in a 50 mL agate jar with 10 agate milling balls, each with a diameter of 10 mm. The rotational speed was set to 200 revolutions per minute (rpm), and the milling time to 30 minutes. After the evaporation of the solvent, the powder was placed in an alumina crucible and heated up to 300 °C, where it was held for 30 hours. Once cooled to room temperature, the brittle solid was ground and homogenized in a mortar. The powder was then placed in an alumina crucible and heated up to 800 °C, held there for 30 hours, and subsequently heated up to 1100 °C, where it was held for an additional 30 hours. For all synthesis steps in the oven, the heating and cooling rate was maintained at 50 °C per hour.

Mechanochemical activation of $NaTi_2(PO_4)_3$. Before sodiation $NaTi_2(PO_4)_3$ was mechanochemically activated by hebm. For this purpose, 3.0 g $NaTi_2(PO_4)_3$ were placed in a 45 mL grinding jar filled with 180 grinding balls (diameter: 5 mm) both consisting of yttrium-stabilized zirconia. The powder was pulverized at a rotational speed of 400 rpm for different time periods (1 h, 2 h, 4 h, 8 h and 16 h) using a PULVERISETTE 7 premium line planetary ball mill (Fritsch, Idar-Oberstein, Germany). The grinding ball to powder ratio here was 23 : 1, and 400 μL of 2-propanol were added as a dispersion agent to prevent powder cementation.

Sodiation of $NaTi_2(PO_4)_3$. In the glovebox, 1.0 g $NaTi_2(PO_4)_3$ (pristine or milled) and 0.48 g anhydrous Na_2S (2.5 equivalents based on mol of the substance, 5 equivalents based on mol of sodium) or in case of NaI 0.93 g anhydrous sodium iodide (2.5 equivalents) were weighed into a dry three-necked flask. After removal from the glovebox, 25 mL of absolute acetonitrile were added under argon counterflow. Afterwards, the reaction mixture was stirred for different time durations (3 h, 6 h, 18 h, 24 h, 48 h, and 96 h) at room temperature under argon.[64] If sodium naphthalene was used, freshly prepared sodium naphthalene dissolved in absolute THF was previously added (5 equivalents) to 1.0 g $NaTi_2(PO_4)_3$ (pristine or milled) and made up to 25 mL total volume with THF, and stirred for the above-mentioned durations.[80,81] The solid obtained was filtered off under argon atmosphere through a frit, washed twice with 15 mL absolute acetonitrile and twice with 50 mL ethanol. The remaining solvent was removed by vacuum, before the solid was stored in the glovebox under inert conditions. For PXRD characterization, a so-called dome sample holder enabled measurements under inert conditions.

Results and discussion

Synthesis of $NaTi_2(PO_4)_3$ applying high-temperature methods

$NaTi_2(PO_4)_3$ was synthesized from the three homogenized reactants (titanium dioxide, diammonium hydrogen phosphate and sodium dihydrogen phosphate) at 1100 °C using a high-temperature method, yielding a white, coarse-grained powder. The product was characterized by PXRD, which confirmed the formation of a phase-pure material with no side phases or impurities (Fig. S1). The sharp reflections in the recorded powder diffractogram indicate that the product is highly crystalline NTP. Rietveld refinement of the PXRD data yielded lattice parameters of $a = 848.7572(15)$ pm and $c = 2179.045(5)$ pm for the rhombohedral crystal structure (space group $R\bar{3}c$). These values are consistent with published data.[7,25,27,29,34,82] The crystallite size of $NaTi_2(PO_4)_3$ was estimated to be 244(2) nm from the PXRD patterns. Further details of the Rietveld refinement and definitions of the *R*-factors are provided in Table S1 of the SI.

The coarse-grained $NaTi_2(PO_4)_3$ obtained by high-temperature synthesis serves as the starting material for the subsequent mechanochemical activation and sodiation experiments.

Mechanochemical activation of $NaTi_2(PO_4)_3$

The MCA of NTP was carried out in a planetary ball mill. Yttrium-stabilized zirconia was used for both the grinding jars and balls. The ball-to-powder ratio was set at 23 : 1, the milling time ranged from 1 hour to 16 hours at a rotational speed of 400 rpm. The parameters used in this study were optimized with regard to the material of the jar, the number of balls and the rotational speed in order to achieve the highest impact force with minimum abrasion. These parameters were adopted for

the current work based on their established effectiveness in similar contexts.

The mechanochemically activated samples were analysed using PXRD. The diffractograms after MCA of NTP only show the typical broadening of the reflections, which is due to the reduction in crystallite size during the grinding process and the strain of the crystalline lattice (Fig. 2a).[83] No additional reflections indicating phase transformation, side phase formation, or impurities were observed. The slight broadening of reflections, quantified by the full width at half maximum (FWHM), is only discernible upon magnification of the PXRD patterns, resulting from decreased crystallite size and strain evolution during milling. After a strong initial decrease from 244(4) nm in the pristine material to 112(2) nm after one hour of milling, the crystallite size only decreases slightly for longer milling times and reaches a size of 66(4) nm after 16 h of milling (Fig. 2b). The crystallite sizes determined for the individual milling durations are listed in Table S2 in the SI. The crystallite size is expected to further decrease with extended milling times, asymptotically approaching a limiting value. This trend is already suggested by the observed behaviour of the crystallite size curve within the investigated time frame of the grinding process. The strain determined *via* Rietveld refinement is found to be zero in the pristine starting material and increases progressively with prolonged milling time, reaching its maximum after 8 hours. However, at an extended milling duration of 16 hours, a slightly reduced strain value is observed compared to that at 8 hours (Fig. 2b). This pattern of strain evolution as a function of milling time has been reported in the literature for several materials, including W, Fe, and WC.[84,85] We have also observed similar behavior in our previous work on the mechanochemical activation of Mn_3O_4.[86] The observed increase and subsequent slight decrease in lattice strain might be explained by two counteracting processes. Initially, mechanical stress during milling likely leads to the formation of defects, which could contribute to an increase in strain. However, as milling continues and crystallite size further reduces, there may be a tendency for long-range stresses to decrease, particularly in very small crystallites. This could potentially account for the observed reduction in strain at extended milling times. The behaviour of different types of defects during the milling process may also play a role in the observed strain evolution. It is possible that point defects (microstrain) persist even in very small nanocrystals, while long-range defects such as dislocations, stacking faults, or micro twinning might be reduced as crystallite size decreases.[87,88] This interpretation could offer a plausible explanation for the complex strain behaviour observed during the milling process.

When treating NTP in the planetary ball mill, the size and morphology of the particles change with increasing milling time. This can be observed in the scanning electron microscopy images (Fig. 3). The SEM images of the pristine starting material produced by high-temperature synthesis show particles with a polyhedron-like geometry, smooth surfaces, and an approximate size of 1 to 4 micrometres. As the grinding process progresses, the particle size decreases, the edges get a sharper profile, and the first signs of particle agglomeration and/or amorphization appear.

Nitrogen physisorption measurements were used to determine the development of the specific surface area (Fig. 2b) at different milling times while maintaining a constant rotational speed of 400 rpm. The pristine starting material has a specific surface area of less than 1 $m^2\ g^{-1}$. After 1 hour milling at 400 rpm, the specific surface increased to 18.6 $m^2\ g^{-1}$, after 2 hours it reached 38.9 $m^2\ g^{-1}$ (Table S2). The surface area remained nearly constant after 4 and 8 hours of milling, reaching a maximum of 40 $m^2\ g^{-1}$ after 4 hours. Prolonged milling beyond this period resulted in a reduction to approximately 12 $m^2\ g^{-1}$ (16 hours). However, the samples have a very small surface area, which makes the measurements subject to

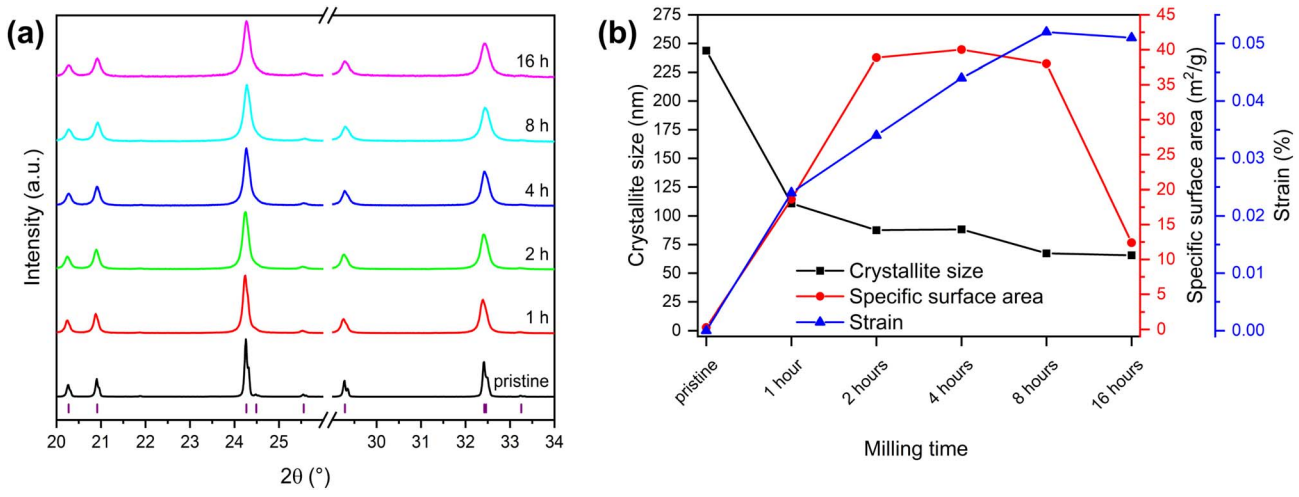

Fig. 2 (a) Enlarged section of normalized PXRD patterns of NTP samples milled at 400 rpm for varying durations. Colored lines correspond to different milling times: black (pristine), red (1 h), green (2 h), dark blue (4 h), light blue (8 h), and pink (16 h). Purple markers indicate the Bragg reflection positions of NTP. (b) Evolution of crystallite size (black squares), specific surface area (red circles), and strain (blue triangles) as a function of milling time, determined *via* Rietveld refinement. Connecting lines are included to guide the eye and illustrate overall trends.

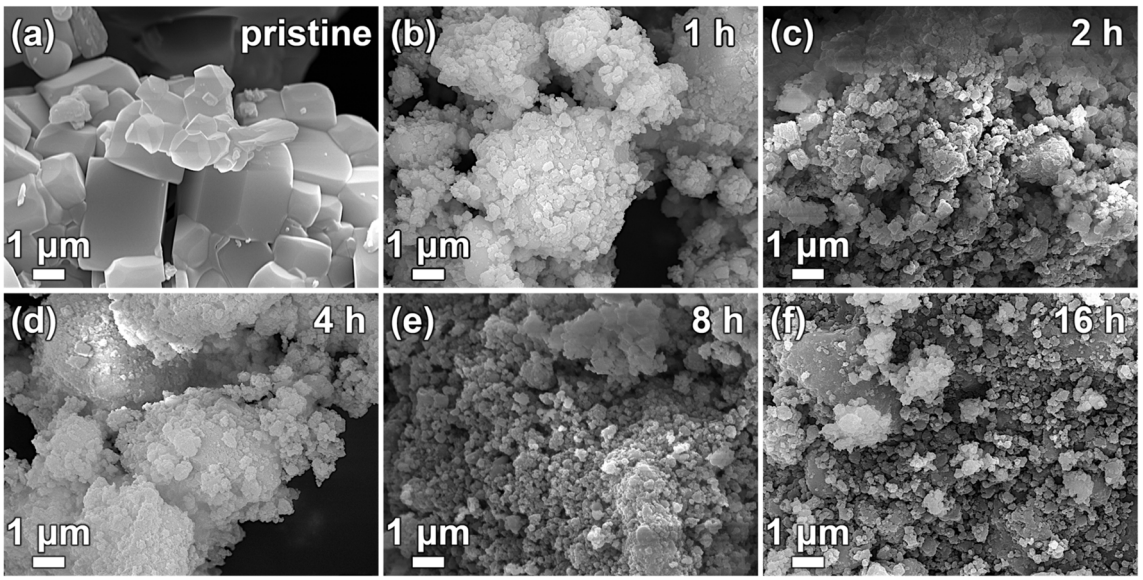

Fig. 3 SEM images of pristine (a) and milled $NaTi_2(PO_4)_3$ at different milling times with constant rotational speed of 400 rpm, 1 hour (b), 2 hours (c), 4 hours (d), 8 hours (e) and 16 hours (f). Factor of magnification 10 000.

error and less suitable for making reliable quantitative statements. Nevertheless, the data shows a general trend of increasing surface area with milling time up to 2–4 hours, followed by a decrease at longer milling times. Corresponding nitrogen physisorption data are presented in the SI (Fig. S2).

The commonly used models for the development of the specific surface during MCA can explain these findings. First, the fragmentation of the particles leads to an increase of the specific surface area, then there is no further increase due to particle aggregation, and finally a decrease in surface area occurs due to the formation of agglomerates or amorphization. This process is consistent with the previously discussed findings on crystallite size reduction and increased strain, reflecting the stages of mechanochemical activation: initial particle breakage, followed by aggregation, and eventual structural disorder or amorphization.[42,89,90]

The input of zirconium and yttrium into the activated material due to abrasion was determined using ICP-MS. In the case of yttrium, this value is below the detection limit. For zirconium, the contend increased from 0.01 wt% at 1 and 2 hours to 0.02 wt% at 4 hours to 0.03 wt% at the two longest milling times of 8 and 16 hours.

Due to two NMR-active nuclei ^{23}Na and ^{31}P, the samples can be analysed by solid-state NMR spectroscopy. Here it is possible to investigate the changes in the local environmental geometry caused by mechanochemical activation. The ^{23}Na spectrum of pristine NTP shows an asymmetric line shape of the central transition $|+1/2\rangle \leftrightarrow |-1/2\rangle$ at $\delta = -7$ ppm due to second order quadrupole interactions, as well as a spinning sideband manifold due to the satellite transitions (Fig. 4a). This can be simulated with a single sodium species. By using the DMFit software quadrupolar parameters of $C_Q = 2920$ kHz and $\eta_Q = 0$ were obtained. For mechanochemically activated NTP, a change in the peak shape is observed. In addition to the quadrupolar broadened signal described before a second sodium species at $\delta = -11$ ppm with a G/L line shape was used to simulate the spectra (Fig. 4b). The simulations for the remaining activation times are shown in the SI (Fig. S3). The shape and position of the signal correspond to the values in the literature.[91–93] As the milling time increases, this broad signal becomes more and more dominant as can be seen in the stacked ^{23}Na NMR spectra, as shown in Fig. 4c. The broad featureless species gives a good hint, that the sodium environment is not ordered anymore, as one would expect because the crystallinity decreases during ball milling. The ^{31}P NMR spectra shows a sharp peak at −27.5 ppm (Fig. 4d), which corresponds to the literature value for crystalline NTP.[94–96] The broad peak in the range between 0 and −25 ppm is due to the slightly altered environmental geometry of the phosphorus atom and is in good agreement with the ^{23}Na spectra. The reason for the changes in the spectra is the slight change in the lattice parameters due to grinding, which becomes stronger with increasing grinding time, due the breaking of bonds, to the formation of amorphous material and reduction of crystallinity.[97]

The Raman spectrum of pristine NTP shows the typical, literature known Raman signals of a phosphate, namely an intense peak at 1010 cm^{-1} (PO_4 symmetric (ν_1) and asymmetric (ν_3) stretching vibrations) and several other, less intense peaks (low-intensity asymmetric (ν_4) and high-intensity symmetric (ν_2), Ti–O bond vibrations and lattice vibrations), in the low frequency range between 100 and 450 cm^{-1}.[70,79,96,98,99] As grinding time progresses, a decrease in peak intensity is observed, likely due to reduced crystallite size and/or increased structural disorder up to amorphization caused by the milling process. At 16 hours of milling, the effect is so great that no significant intensity of the peaks can be found.[100] The corresponding Raman spectra are shown in the SI (Fig. S4).

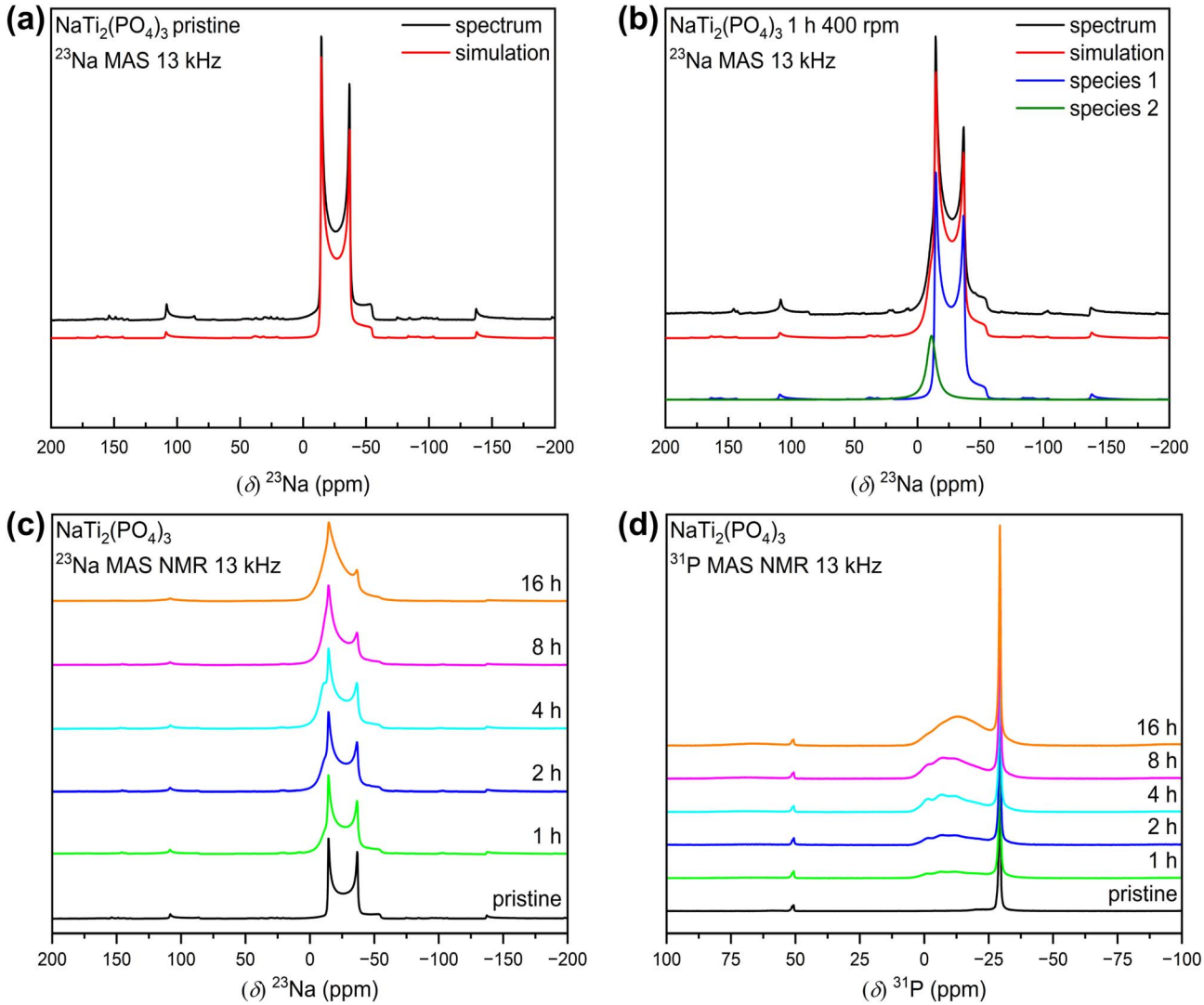

Fig. 4 ^{23}Na and ^{31}P MAS NMR spectra of pristine and milled NTP. (a and b) Experimental spectra (black) and corresponding simulations (red). In (b), the simulation includes the quadrupolar contribution of the pristine material (blue) and the G/L species formed upon milling (green). (c and d) Evolution of the ^{23}Na and ^{31}P spectra with increasing milling duration. Colored lines represent different milling times: black (pristine), green (1 h), dark blue (2 h), light blue (4 h), pink (8 h), and orange (16 h).

Mechanochemical activation significantly affects material properties, including particle and crystallite size, specific surface area, and structural disorder, which in turn influence diffusion phenomena in solid-state chemistry and intercalation processes. These changes are evident in NTP through various characterization techniques.

Sodiation of $NaTi_2(PO_4)_3$

To investigate the influence of the changes in the material caused by MCA described above, sodiation experiments were carried out on mechanochemically activated samples. The general formula for sodium intercalation in NTP is shown in Scheme 1. The reactions were carried out in suspension, sodium naphthalene (NaNaph), sodium sulphide (Na_2S) and sodium iodide (NaI) were used as sodium sources. THF was used as a solvent for NaNaph and acetonitrile for Na_2S and NaI. For each sodium cation that is incorporated into the host structure, an electron is simultaneously transferred. This leads to the reduction of the two titanium atoms. Up to three sodium atoms can be inserted into the starting material, reducing the two titanium atoms from an initial oxidation state of 4+ to a mixed-valent 2+/3+ state in the product $Na_4Ti_2(PO_4)_3$.

Kinetic studies were performed to determine the influence of MCA on the intercalation of sodium in NTP. The same initial

$$NaTi_2(PO_4)_3 + \text{Na-Source} \xrightarrow[0 \le x \le 3]{\text{Solvent}} Na_{1+x}Ti_2(PO_4)_3$$

Na-Source: Na-naphthalene, Na_2S, NaI Solvents: acetonitrile, THF

Scheme 1 General reaction equation for the sodiation of $NaTi_2(PO_4)_3$ with different sodium compounds (NaNaph, Na_2S, NaI). The reactions were carried out in suspensions using either THF or acetonitrile as the solvent.

sodium concentration was used for all experiments to allow comparison of the individual series. Pristine and mechanochemically activated NTP was stirred with 5 equivalents (based on sodium) of different sodium sources (NaNaph, Na_2S, NaI) in a constant amount of solvent (25 mL) for different periods of time. When using NaI, only 2.5 equivalents were used, to avoid problems with stirring and work-up due to the high molar mass and the resulting high initial weight. The mixtures were filtered under argon, the sodium source was quenched, and the products were washed, before being analysed by PXRD. All steps were carried out under inert conditions to prevent undesired reactions with air and/or moisture. The average sodium content of the samples was calculated from the sodium content of the individual phases and their weight fraction was determined by Rietveld refinement. The three literature-known phases of $Na_{1+x}Ti_2(PO_4)_3$ ($x = 0$, 2, 3) served as the basis for the Rietveld refinement; there is no evidence for the formation of $Na_2Ti_2(PO_4)_3$, likely due to its tendency to disproportionate. The reactivity of the sodium sources follows the order of their reduction potentials: NaNaph (~ -2.4 V) has the highest reactivity, followed by Na_2S (~ -0.48 V) and NaI (~ 0.54 V) has the lowest reactivity. The electrochemical series has a value of -0.055 V for the reduction of Ti^{4+} to Ti^{3+} and a value of -0.369 V for the reduction of Ti^{3+} to Ti^{2+}.[62,101] The values provided are intended as guidelines rather than absolute measurements. These values were derived from various standards and subsequently converted for comparison. It should be noted that the experimental setups described in the literature differ from that employed in this study, particularly with respect to the solvents used and their concentrations. Nevertheless, the reactivity gradation observed in our tested system can be approximated based on the literature values.

For the first kinetic study, Na_2S was used as the sodium source with acetonitrile as the solvent. Here, the average sodium content ($\langle x \rangle$) in $Na_xTi_2(PO_4)_3$, defined as the mean number of sodium atoms per formula unit, was determined for both pristine and mechanochemically activated NTP samples and compared after stirring for different times at room temperature. The sodium content as a function of the reaction parameters is shown in Fig. 5a, and the obtained PXRD patterns for the sodiation of milled NTP (4 hours, 400 rpm) are exemplarily shown in Fig. 5b. Pristine NTP shows no significant sodium intercalation even after 96 hours; the average sodium content is 1.02, meaning that sodium intercalation is negligible under the tested conditions. An increase in the sodium content can be observed in all mechanochemically activated samples with short sodiation times (up to 18 hours). The highest values, with a sodium content of approx. 2.2 (at 18 hours stirring time) were achieved with the samples activated for 2 hours. In contrast, at an activation time of 16 hours, the lowest value of 1.3 was determined at 18 hours stirring time. With prolonged sodiation time (up to 48 hours), only a slight increase in sodium content is observed in all activated samples except for the sample with an activation time of 4 hours. From this point onwards, no significant further incorporation of sodium into NTP appears to take place in these samples. Shorter activation times of 1 or 2 hours result in higher sodium uptake in NTP. Longer activation times of 8 or 16 hours also improve sodium intercalation compared to the pristine starting material, but to a lesser extent than shorter activation times. One exception is the sample that was mechanochemically activated for 4 hours. This sample shows an almost constant increase in sodium content over the entire sodiation time of 96 hours, reaching a sodium content of nearly 3 after this time. To determine the maximum possible sodium content under these reaction conditions, further reactions with longer reaction times (8 and 16 days) were carried out using this activated sample. A sodium content of exactly 3 was achieved in both experiments and there is no evidence in the PXRD pattern to indicate the formation of the $Na_4Ti_2(PO_4)_3$ phase. This means that when NTP is sodiated at room temperature with Na_2S in acetonitrile, a maximum value of 3.0 can be achieved for the average sodium content. NTP must first be activated for 4 hours at 400 rpm and Na_2S is not able to reduce Ti^{3+} to Ti^{2+}. The remaining PXRDs are shown in the SI (Fig. S5–S10). One possible explanation for the observed sodium values is the evolution of the specific surface area with the milling time. Pristine NTP has a very low surface area and large crystals, resulting in long diffusion paths for the sodium cations. With longer milling times, the surface area increases, while the crystal size decreases, facilitating the intercalation of sodium.

The best sodium intercalation properties of NTP achieved with Na_2S and an activation time of 4 hours are in excellent agreement with the BET results as the largest specific surface area is observed after 4 hours of milling. Activation times of more than 4 hours lead to lower sodium values, as the aggregation/agglomeration or amorphization of the particles and the strain increase significantly, making intercalation in NTP more difficult.

In a further study, the influence of the sodium source on the sodium content in the NTP was investigated. Sodium naphthalene was used as a more reactive sodium source, as its reduction potential is larger than that of Na_2S. The reaction conditions were kept the same as in the experiments with sodium sulphide described above, but a different solvent, namely THF, had to be used.

The PXRD patterns of the obtained products after sodiation with NaNaph show that in addition to the $Na_3Ti_2(PO_4)_3$ phase, $Na_4Ti_2(PO_4)_3$ is also formed when using NaNaph as the sodium source (Fig. 6 and S11–S15). This highly sodiated phase must be considered in the Rietveld refinement and the determination of the sodium content. A comparison between sodium naphthalene (NaNaph) and sodium sulfide (Na_2S) as sodiation agents reveals that NaNaph, due to its higher reactivity, facilitates greater sodium incorporation into the $NaTi_2(PO_4)_3$ structure. Samples treated with NaNaph exhibit an average sodium content ranging from approximately 2.7 to 3.4 after just 3 hours of reaction time. Beyond this point, only marginal increases in sodium content are observed with extended reaction durations, and no significant enhancement is detected after 48 hours. This plateau suggests that a saturation point is reached under the given conditions, indicating that the maximum achievable sodium intercalation has been attained. A comparison between the pristine and the mechanochemically activated samples

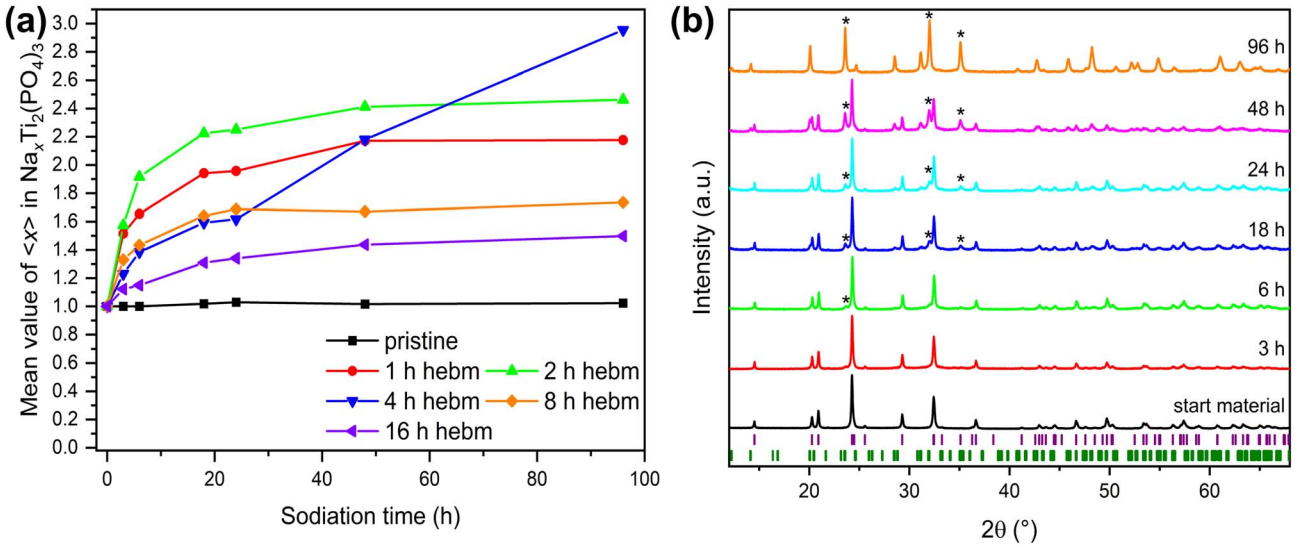

Fig. 5 (a) Mean value ⟨*x*⟩ of $Na_xTi_2(PO_4)_3$ determined by Rietveld refinement, shown as a function of milling duration at 400 rpm and subsequent sodiation time. Milling durations are indicated by colored lines: black (pristine), red (1 h), green (2 h), blue (4 h), orange (8 h), and purple (16 h). Sodiation was performed using 2.5 equivalents of sodium sulfide in acetonitrile for varying durations (3 h, 6 h, 18 h, 24 h, 48 h, and 96 h). (b) Enlarged section of normalized PXRD patterns of selected sodiated samples, exemplified by NTP milled for 4 h at 400 rpm and sodiated for different time intervals. Colored lines represent sodiation times: black (0 h), red (3 h), green (6 h), dark blue (18 h), light blue (24 h), pink (48 h), and orange (96 h). Bragg positions of $NaTi_2(PO_4)_3$ and $Na_3Ti_2(PO_4)_3$ are indicated by purple and green lines, respectively. Asterisks (*) mark characteristic reflections of $Na_3Ti_2(PO_4)_3$.

shows that the pristine sample has the highest sodium content of around 3.5 after 96 hours, while the sample with 1 hour of activation only shows a value of 3.3. Overall, sodium intercalation decreases continuously with increasing activation time, *i.e.* the sample activated for the longest time exhibits the lowest value of 3.0 after 96 hours. This suggests that when using NaNaph, the intercalation is greatest if the sample is not mechanochemically activated. The longer the activation of the samples, the less sodium intercalates. A possible explanation for the highest sodium content when using pristine NTP could be the low degree of dissociation of NaNaph in THF. The strain, formation of aggregates/agglomerates, or amorphization may

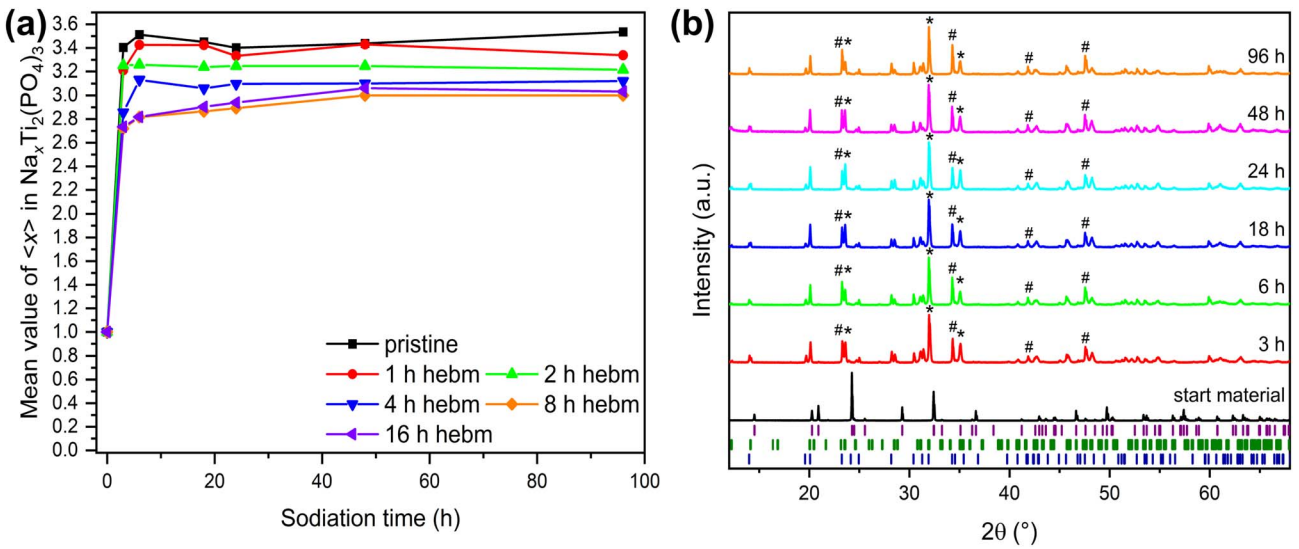

Fig. 6 (a) Mean value ⟨*x*⟩ of $Na_xTi_2(PO_4)_3$ determined by Rietveld refinement, shown as a function of milling duration at 400 rpm and subsequent sodiation time. Milling durations are indicated by colored lines: black (pristine), red (1 h), green (2 h), blue (4 h), orange (8 h), and purple (16 h). Sodiation was performed using 5 equivalents of sodium naphthalene in THF for varying durations (3 h, 6 h, 18 h, 24 h, 48 h, and 96 h). (b) Enlarged section of normalized PXRD patterns of selected sodiated samples, exemplified by pristine NTP and sodiated for different time intervals. Colored lines represent sodiation times: black (0 h), red (3 h), green (6 h), dark blue (18 h), light blue (24 h), pink (48 h), and orange (96 h). Bragg positions of $NaTi_2(PO_4)_3$, $Na_3Ti_2(PO_4)_3$, and $Na_4Ti_2(PO_4)_3$ are marked in purple, green, and blue, respectively. Asterisks (*) and hash symbols (#) mark characteristic reflections of $Na_3Ti_2(PO_4)_3$ and $Na_4Ti_2(PO_4)_3$, respectively.

hinder the diffusion of the solvated ion pair, resulting in less sodium intercalation.[62] These effects become more pronounced with increasing milling time. The $Na_4Ti_2(PO_4)_3$ phase is only formed with NaNaph and is not visible in the PXRD patterns when using Na_2S under the tested conditions. The reasons for this could lie in the reduction potential of the two different sodium sources, since only NaNaph is likely able to further reduce Ti^{3+} to Ti^{2+}. Further attempts were made to obtain the pure $Na_4Ti_2(PO_4)_3$ phase without the $Na_3Ti_2(PO_4)_3$ phase, using 10 equivalents of NaNaph and by post-sodiation of an already sodiated phase. However, no higher sodium content was achieved in either case, *i.e.* the $Na_4Ti_2(PO_4)_3$ phase is present simultaneously with the $Na_3Ti_2(PO_4)_3$ phase under the investigated conditions. The $Na_4Ti_2(PO_4)_3$ phase can be synthesized *via* the electrochemical route, as described in the literature.[16]

In addition to Rietveld refinement, the sodium content of selected samples was quantified using ICP-MS. The results exhibit a similar trend to those obtained *via* Rietveld analysis; however, the sodium values determined by ICP-MS are consistently slightly higher, particularly in samples sodiated with Na_2S. This discrepancy likely arises from the fundamental differences in the measurement principles of the two techniques. ICP-MS determines the total sodium-to-titanium ratio, which includes not only intercalated sodium but also any sodium species adsorbed on particle surfaces or incorporated into amorphous phases generated during milling—both of which are undetectable by PXRD. Consequently, ICP-MS may overestimate the amount of intercalated sodium. In contrast, Rietveld refinement selectively quantifies sodium incorporated into the crystalline lattice. The corresponding data are provided in the SI (Table S3).

The third sodium source investigated was sodium iodide, which possesses a lower reduction potential compared to sodium naphthalene (NaNaph) and sodium sulfide (Na_2S). Since activation of NTP for 4 hours at 400 rpm resulted in the highest intercalation of sodium when Na_2S was used and the use of NaNaph resulted in the highest sodium content when pristine starting material was used, these two NTP samples were stirred with NaI in acetonitrile at room temperature for 96 hours, before being analyzed. No intercalation of sodium was observed in either experiment, *i.e.* sodium iodide is not able to reduce the Ti^{4+} and incorporate sodium into the host structure under the conditions tested. The corresponding PXRDs are shown in the SI (Fig. S16).

Consequently, the amount of sodium intercalated in NTP depends on two factors: the sodiation agent (influenced by its reduction potential) and whether the sample underwent mechanochemical activation (MCA) or not.

Due to its low reduction potential, the use of NaI did not result in any sodium incorporation into NTP under the tested conditions. However, MCA of NTP resulted in an improved sodium uptake with Na_2S as sodiation agent. Milling for 4 hours was found to be the optimal condition for MCA, resulting in a sodium content of 3.0. Higher values were not achieved, as Na_2S likely cannot further reduce the titanium. NaNaph led to the highest sodium contents, sometimes exceeding 3.5 and forming the most sodium-rich phase $Na_4Ti_2(PO_4)_3$. However, phase-pure $Na_4Ti_2(PO_4)_3$ did not form under these conditions. Surprisingly, MCA appeared to hinder sodium incorporation with NaNaph.

Conclusions

This study investigated the influence of mechanochemical activation of coarse-grained sodium titanium phosphate (NTP) on physical parameters, such as crystallite size and specific surface area, and the subsequent impact on sodium intercalation using different sodium sources. The coarse-grained starting material was synthesized by high-temperature synthesis and then milled for various durations in a planetary ball mill at a rotational speed of 400 rpm. The reduction in crystallite size due to grinding was confirmed by Rietveld refinement of PXRD data, Raman spectroscopy, and SEM images, with values decreasing from 244(4) nm (pristine) to the lowest measured value of 66(4) nm after 16 hours milling. Nitrogen physisorption was used to measure the evolution of specific surface area with milling duration, revealing values increasing from less than 1 $m^2\ g^{-1}$ (pristine) to a maximum of 40 $m^2\ g^{-1}$ after 4 hours milling, followed by a decline to 12 $m^2\ g^{-1}$ at 16 hours. Both the Raman spectra and the MAS NMR spectra of the two NMR-active nuclei show a change in the local environment of the atoms due to the grinding. This is evidenced by shifts and changes in the spectral features, which arise from a gradual alteration of the lattice parameters, reduced crystallite size and structural disorder as mechanical stress is applied during grinding. Kinetic studies investigating the influence of activation on intercalation behavior were carried out using chemical sodiation with various sodium sources (Na_2S, NaNaph, NaI) in suspension. The type of sodium species used, and its reduction potential determine whether and, if so, to what extent. No sodium intercalation is observed when NaI is used. In the case of NaNaph, the highest sodium values, up to 3.5, are achieved when pristine NTP is sodiated, indicating that MCA poses a greater obstacle to intercalation in this instance. Contrary, a strong improvement in the intercalation of sodium in NTP was observed for Na_2S. Hereby, the most effective activation is reached after 4 hours of milling and a sodium content of 3.0 was achieved. Higher values are not obtained, probably because Na_2S cannot further reduce the titanium atom. Overall, these findings demonstrate that while MCA can enhance sodium intercalation in NTP, its effectiveness is highly dependent on the interplay between structural modifications and the chemical nature of the sodiation agent. Optimizing both parameters is essential for tailoring NASICON-type materials for high-performance sodium-ion storage applications.

Conflicts of interest

The authors declare no competing financial interest.

Data availability

The additional data supporting this article have been included as a part of supplementary information (SI). Supplementary

information: characterization of the obtained materials, including structure refinement parameters, crystallite size, specific surface, physisorption isotherms, ^{23}Na and ^{31}P CP-MAS NMR spectra, Raman spectra, PXRD, ICP-MS data. See DOI: https://doi.org/10.1039/d5mr00090d.

Acknowledgements

Instrumentation and technical assistance for this work were provided by the Service Center X-ray Diffraction, with financial support from Saarland University and German Science Foundation (project number INST 256/349-1) and by the Service Center NMR with financial support from Saarland University and German Research Foundation DFG. ICP-MS instrumentation for this work was provided by the elemental analysis group, with financial support from Saarland University and German Science Foundation (project number: INST 256/553-1). We would like to thank Dr Stefan Engel for recording the SEM, Aaron Haben for the elemental quantification *via* ICP-MS, Sarah Schumacher and Dr Peter William de Oliveira at the INM – Leibniz Institute for New Materials in Saarbrücken (Germany) for the nitrogen physisorption measurements. The authors declare they have used DeepL translator as an Artificial Intelligence (AI) tool for the polishing of the language.

References

1 Z. Xu and J. Wang, *Adv. Energy Mater.*, 2022, **12**, 2201692.
2 C. B. Tabelin, J. Dallas, S. Casanova, T. Pelech, G. Bournival, S. Saydam and I. Canbulat, *Miner. Eng.*, 2021, **163**, 106743.
3 C.-X. Zu and H. Li, *Energy Environ. Sci.*, 2011, **4**, 2614–2624.
4 H. Pan, Y.-S. Hu and L. Chen, *Energy Environ. Sci.*, 2013, **6**, 2338–2360.
5 F. Li, Z. Wei, A. Manthiram, Y. Feng, J. Ma and L. Mai, *J. Mater. Chem. A*, 2019, **7**, 9406–9431.
6 B. L. Ellis and L. F. Nazar, *Curr. Opin. Solid State Mater. Sci.*, 2012, **16**, 168–177.
7 L.-O. Hagman, P. Kierkegaard, P. Karvonen, A. I. Virtanen and J. Paasivirta, *Acta Chem. Scand.*, 1968, **22**, 1822–1832.
8 M. Šljukić, B. Matković, B. Prodić and S. Ščavnićar, *Croat. Chem. Acta*, 1967, **39**, 145–148.
9 K. C. Sobha and K. J. Rao, *J. Solid State Chem.*, 1996, **121**, 197–201.
10 L. Vijayan and G. Govindaraj, *Physica B*, 2009, **404**, 3539–3543.
11 Z.-E. Yu, Y. Lyu, Z. Zou, N. Su, B. He, S. Wang, S. Shi and B. Guo, *ACS Sustainable Chem. Eng.*, 2021, **9**, 13414–13423.
12 C. Delmas, A. Nadiri and J. L. Soubeyroux, *Solid State Ionics*, 1988, **28–30**, 419–423.
13 A. El Jazouli, A. Nadiri, J. M. Dance, C. Delmas and G. Le Flem, *J. Phys. Chem. Solids*, 1988, **49**, 779–783.
14 H. Kabbour, D. Coillot, M. Colmont, C. Masquelier and O. Mentré, *J. Am. Chem. Soc.*, 2011, **133**, 11900–11903.
15 A. K. Padhi, K. S. Nanjundaswamy, C. Masquelier and J. B. Goodenough, *J. Electrochem. Soc.*, 1997, **144**, 2581.
16 P. Senguttuvan, G. Rousse, M. E. Arroyo y de Dompablo, H. Vezin, J. M. Tarascon and M. R. Palacín, *J. Am. Chem. Soc.*, 2013, **135**, 3897–3903.
17 T. Stüwe, D. Werner, D. Stock, C. W. Thurner, A. Thöny, C. Grießer, T. Loerting and E. Portenkirchner, *Batteries Supercaps*, 2023, **6**, e202300228.
18 J. B. Goodenough, H. Y. P. Hong and J. A. Kafalas, *Mater. Res. Bull.*, 1976, **11**, 203–220.
19 C. Delmas, J.-C. Viala, R. Olazcuaga, G. Le Flem, P. Hagenmuller, F. Cherkaoui and R. Brochu, *Solid State Ionics*, 1981, **3–4**, 209–214.
20 L. Wang, Z. Huang, B. Wang, G. Liu, M. Cheng, Y. Yuan, H. Luo, T. Gao, D. Wang and R. Shahbazian-Yassar, *ACS Appl. Mater. Interfaces*, 2019, **11**, 10663–10671.
21 R. Shannon, *Acta Crystallogr., Sect. A:Found. Crystallogr.*, 1976, **32**, 751–767.
22 S. Chen, C. Wu, L. Shen, C. Zhu, Y. Huang, K. Xi, J. Maier and Y. Yu, *Adv. Mater.*, 2017, **29**, 1700431.
23 B. Wang, T. Liu, A. Liu, G. Liu, L. Wang, T. Gao, D. Wang and X. S. Zhao, *Adv. Energy Mater.*, 2016, **6**, 1600426.
24 E. J. Kim, P. R. Kumar, Z. T. Gossage, K. Kubota, T. Hosaka, R. Tatara and S. Komaba, *Chem. Sci.*, 2022, **13**, 6121–6158.
25 Z. Li, D. Young, K. Xiang, W. C. Carter and Y.-M. Chiang, *Adv. Energy Mater.*, 2013, **3**, 290–294.
26 G. Pang, P. Nie, C. Yuan, L. Shen, X. Zhang, H. Li and C. Zhang, *J. Mater. Chem. A*, 2014, **2**, 20659–20666.
27 G. Pang, C. Yuan, P. Nie, B. Ding, J. Zhu and X. Zhang, *Nanoscale*, 2014, **6**, 6328–6334.
28 S. I. Park, I. Gocheva, S. Okada and J.-i. Yamaki, *J. Electrochem. Soc.*, 2011, **158**, A1067.
29 D. Wang, Q. Liu, C. Chen, M. Li, X. Meng, X. Bie, Y. Wei, Y. Huang, F. Du, C. Wang and G. Chen, *ACS Appl. Mater. Interfaces*, 2016, **8**, 2238–2246.
30 G. Yang, H. Song, M. Wu and C. Wang, *J. Mater. Chem. A*, 2015, **3**, 18718–18726.
31 J. Yang, H. Wang, P. Hu, J. Qi, L. Guo and L. Wang, *Small*, 2015, **11**, 3744–3749.
32 F. d'Yvoire, M. Pintard-Scrépel, E. Bretey and M. de la Rochère, *Solid State Ionics*, 1983, **9–10**, 851–857.
33 M. de la Rochère, F. d'Yvoire, G. Collin, R. Comès and J. P. Boilot, *Solid State Ionics*, 1983, **9–10**, 825–828.
34 J. L. Rodrigo and J. Alamo, *Mater. Res. Bull.*, 1991, **26**, 475–480.
35 C. Delmas, F. Cherkaoui, A. Nadiri and P. Hagenmuller, *Mater. Res. Bull.*, 1987, **22**, 631–639.
36 D. Gryaznov, S. K. Stauffer, E. A. Kotomin and L. Vilčiauskas, *Phys. Chem. Chem. Phys.*, 2020, **22**, 11861–11870.
37 H. Güler and F. Kurtuluş, *Mater. Chem. Phys.*, 2006, **99**, 394–397.
38 V. Pet'kov, V. N. Loshkarev, A. I. Orlova, V. S. Kurazhkovskaya and V. T. Demarin, *Russ. J. Inorg. Chem.*, 2002, **47**, 1053–1057.
39 Z. Wang, J. Liang, K. Fan, X. Liu, C. Wang and J. Ma, *Front. Chem.*, 2018, **6**, 396.
40 A. F. Fuentes and L. Takacs, *J. Mater. Sci.*, 2013, **48**, 598–611.

41 J. L. Howard, Q. Cao and D. L. Browne, *Chem. Sci.*, 2018, **9**, 3080–3094.
42 I. Tole, K. Habermehl-Cwirzen and A. Cwirzen, *Mineral. Petrol.*, 2019, **113**, 449–462.
43 H. He, G. Di, X. Gao and X. Fei, *Chemosphere*, 2020, **243**, 125339.
44 D. Tan and F. García, *Chem. Soc. Rev.*, 2019, **48**, 2274–2292.
45 D. Becker, M. Klos and G. Kickelbick, *Inorg. Chem.*, 2019, **58**, 15021–15024.
46 D. Becker, R. Haberkorn and G. Kickelbick, *Inorganics*, 2018, **6**, 117.
47 S. R. Chauruka, A. Hassanpour, R. Brydson, K. J. Roberts, M. Ghadiri and H. Stitt, *Chem. Eng. Sci.*, 2015, **134**, 774–783.
48 Y. Chen, J. Fitz Gerald, L. T. Chadderton and L. Chaffron, *Appl. Phys. Lett.*, 1999, **74**, 2782–2784.
49 K. O. Hara, E. Yamasue, H. Okumura and K. N. Ishihara, *J. Phys.:Conf. Ser.*, 2009, **144**, 012021.
50 H. Yang and H. Bakker, *Mater. Sci. Eng., A*, 1994, **181–182**, 1207–1211.
51 D. Becker, R. Haberkorn and G. Kickelbick, *Eur. J. Inorg. Chem.*, 2019, **2019**, 4835–4845.
52 N. R. Rightmire and T. P. Hanusa, *Dalton Trans.*, 2016, **45**, 2352–2362.
53 S. L. James, C. J. Adams, C. Bolm, D. Braga, P. Collier, T. Friščić, F. Grepioni, K. D. M. Harris, G. Hyett, W. Jones, A. Krebs, J. Mack, L. Maini, A. G. Orpen, I. P. Parkin, W. C. Shearouse, J. W. Steed and D. C. Waddell, *Chem. Soc. Rev.*, 2012, **41**, 413–447.
54 G. F. Goya and H. R. Rechenberg, *J. Magn. Magn. Mater.*, 1999, **203**, 141–142.
55 L. Kocsor, L. Péter, G. Corradi, Z. Kis, J. Gubicza and L. Kovács, *Crystals*, 2019, **9**, 334.
56 Y. Yang, S. Zhang, S. Wang, K. Zhang, H. Wang, J. Huang, S. Deng, B. Wang, Y. Wang and G. Yu, *Environ. Sci. Technol.*, 2015, **49**, 4473–4480.
57 L. Guo, Z. Hu, Y. Du, T. C. Zhang and D. Du, *J. Hazard. Mater.*, 2021, **414**, 125436.
58 Y. Huang, X. Li, J. Luo, K. Wang, Q. Zhang, Y. Qiu, S. Sun, S. Liu, J. Han and Y. Huang, *ACS Appl. Mater. Interfaces*, 2017, **9**, 8696–8703.
59 I. R. Speight and T. P. Hanusa, *Molecules*, 2020, **25**, 570.
60 M. Wang, Q. Tan and J. Li, *Environ. Sci. Technol.*, 2018, **52**, 13136–13143.
61 M. Avdeev, Z. Mohamed, C. D. Ling, J. Lu, M. Tamaru, A. Yamada and P. Barpanda, *Inorg. Chem.*, 2013, **52**, 8685–8693.
62 N. G. Connelly and W. E. Geiger, *Chem. Rev.*, 1996, **96**, 877–910.
63 M. Galceran, D. Saurel, B. Acebedo, V. V. Roddatis, E. Martin, T. Rojo and M. Casas-Cabanas, *Phys. Chem. Chem. Phys.*, 2014, **16**, 8837–8842.
64 R. Haberkorn, J. Bauer and G. Kickelbick, *Z. Anorg. Allg. Chem.*, 2014, **640**, 3197–3202.
65 Y. Liu, X. Wu, A. Moeez, Z. Peng, Y. Xia, D. Zhao, J. Liu and W. Li, *Adv. Energy Mater.*, 2023, **13**, 2203283.
66 M. Xu, F. Zhang, Y. Zhang, C. Wu, X. Zhou, X. Ai and J. Qian, *Chem. Sci.*, 2023, **14**, 12570–12581.
67 A. u. I. Gebi, O. Dolokto, L. Mereacre, U. Geckle, H. Radinger, M. Knapp and H. Ehrenberg, *ChemSusChem*, 2024, **17**, e202300809.
68 H. Morimoto, H. Awano, J. Terashima, Y. Shindo, S. Nakanishi, N. Ito, K. Ishikawa and S.-i. Tobishima, *J. Power Sources*, 2013, **240**, 636–643.
69 Z. Li, D. B. Ravnsbæk, K. Xiang and Y.-M. Chiang, *Electrochem. Commun.*, 2014, **44**, 12–15.
70 G. Snarskis, J. Pilipavičius, D. Gryaznov, L. Mikoliūnaitė and L. Vilčiauskas, *Chem. Mater.*, 2021, **33**, 8394–8403.
71 M. K. Chong, Z. Zainuddin, F. S. Omar and M. H. H. Jumali, *Ceram. Int.*, 2022, **48**, 22106–22113.
72 X. Li, Y. Zhou, J. Tang, S. Zhao, J. Zhang, X. Huang and B. Tian, *ACS Appl. Mater. Interfaces*, 2023, **15**, 36289–36300.
73 S. A. Novikova, A. B. Il'in, N. A. Zhilyaeva and A. B. Yaroslavtsev, *Inorg. Mater.*, 2018, **54**, 676–682.
74 *Topas V5.0*, Bruker AXS, Karlsruhe, Germany, 2014.
75 P. Villars and K. Cenzual, Pearson's Crystal Data: Crystal Structure Database for Inorganic Compounds (on DVD), Release 2022/23, ASM International®, Materials Park, Ohio, USA.
76 *TopSpin V2.1*, Bruker, Karlsruhe, Germany, 2008.
77 D. Massiot, F. Fayon, M. Capron, I. King, S. Le Calvé, B. Alonso, J.-O. Durand, B. Bujoli, Z. Gan and G. Hoatson, *Magn. Reson. Chem.*, 2002, **40**, 70–76.
78 K. Brandenburg and M. Berndt, *Diamond V4.6.8.*, Crystal Impact GbR, Bonn, Germany, 2022.
79 C. E. Bamberger, G. M. Begun and O. B. Cavin, *J. Solid State Chem.*, 1988, **73**, 317–324.
80 P. G. Bruce and G. Miln, *J. Solid State Chem.*, 1990, **89**, 162–166.
81 S. Zhou, G. Barim, B. J. Morgan, B. C. Melot and R. L. Brutchey, *Chem. Mater.*, 2016, **28**, 4492–4500.
82 J. L. Rodrigo, P. Carrasco and J. Alamo, *Mater. Res. Bull.*, 1989, **24**, 611–618.
83 A. C. Murrieta and F. F. Contreras-Torres, *Mater. Today: Proc.*, 2022, **48**, 96–100.
84 A. I. Gusev and A. S. Kurlov, *Nanotechnology*, 2008, **19**, 265302.
85 D. Oleszak and P. H. Shingu, *J. Appl. Phys.*, 1996, **79**, 2975–2980.
86 T. B. Straub, R. Haberkorn and G. Kickelbick, *Inorg. Chem.*, 2025, **64**, 6420–6433.
87 P. K. Giri, *J. Phys. D: Appl. Phys.*, 2009, **42**, 245402.
88 C. C. Koch, *Nanostruct. Mater.*, 1997, **9**, 13–22.
89 M. Francke, H. Hermann, R. Wenzel, G. Seifert and K. Wetzig, *Carbon*, 2005, **43**, 1204–1212.
90 L. Opoczky, *Powder Technol.*, 1977, **17**, 1–7.
91 H. Bradtmüller, A. M. Nieto-Muñoz, J. F. Ortiz-Mosquera, A. C. M. Rodrigues and H. Eckert, *J. Non-Cryst. Solids*, 2018, **489**, 91–101.
92 H. Masui, T. Ueda, K. Miyakubo, T. Eguchi and N. Nakamura, *Z. Naturforsch.*, 2000, **55**, 348–352.
93 S. Yu, Z. Liu, H. Tempel, H. Kungl and R.-A. Eichel, *J. Mater. Chem. A*, 2018, **6**, 18304–18317.
94 Y. Bereznitski, M. Jaroniec, A. I. Bortun, D. M. Poojary and A. Clearfield, *J. Colloid Interface Sci.*, 1997, **191**, 442–448.

95 C. Schmutz, P. Barboux, F. Ribot, F. Taulelle, M. Verdaguer and C. Fernandez-Lorenzo, *J. Non-Cryst. Solids*, 1994, **170**, 250–262.
96 Y. Yue and W. Pang, *Mater. Res. Bull.*, 1990, **25**, 841–844.
97 R. Borges, V. Prevot, C. Forano and F. Wypych, *Ind. Eng. Chem. Res.*, 2017, **56**, 708–716.
98 P. Tarte, A. Rulmont and C. Merckaert-Ansay, *Spectrochim. Acta, Part A*, 1986, **42**, 1009–1016.
99 Y. Yong and P. Wenqin, *J. Chem. Soc., Chem. Commun.*, 1990, 764–765.
100 T. Rojac, B. Malič, M. Kosec, M. Połomska, B. Hilczer, B. Zupančič and B. Zalar, *Solid State Ionics*, 2012, **215**, 1–6.
101 J. R. Rumble, D. R. Lide and T. J. Bruno, *CRC Handbook of Chemistry and Physics*, CRC Press, Boca Raton, FL, 98th edn, 2017.